Proceedings of the Second International Workshop on EGS, 8.-12. August 2000, Tsukuba, Japan
KEK Proceedings 200-20, pp.92-99

Optimization of PET Scanner Geometry

Lars-Eric Adam and J. S. Karp

Department of Radiology, University of Pennsylvania
3400 Spruce Street, Philadelphia, PA 19104, U.S.A.

Abstract

Modern positron emission tomographs (PET), when used for 3D imaging, have a wide open gantry without intra plane septa and only little shielding. In order to reduce the scatter contamination from activity inside and outside the field-of-view (FOV), and to block radiation originating from activity outside-the-FOV, we have investigated the implementation of septa and additional patient shielding on our existing whole body PET scanner. A series of Monte Carlo simulations, based on EGS4, were performed to predict the potential benefits. Our simulations include point and line sources at various radial and axial positions in the FOV of the scanner, and different sized uniform cylinders (up to 100 cm long and 50 cm in diameter). The scanner itself is based on 6 continuous NaI(Tl) crystals, an axial FOV of 25.6 cm, a ring diameter of 90 cm, and a transaxial FOV of 56 cm. The results show that septa can reduce the relative scatter fraction and effectively block radiation from outside-the-FOV, but they also reduce the sensitivity for true events, leading to a decrease of the trues-to-singles ratio that is not desirable. The use of septa is only advantageous for large objects, if the loss of true events is compensated for by increasing the injected activity. Patient shields that are mounted outside-the-FOV reduce the contamination from scattered and single events without interfering with true events. They are more effective for objects with a small diameter and less effective for objects with a large diameter.

1 Introduction

The strength of positron emission tomography (PET) is the ability to quantify the activity distribution of radionuclides in the human body. During the data acquisition, a considerable amount of the emission photons are scattered and/or attenuated within the patient body, which leads to an error of the measurement that requires correction methods. With the new generation of 3D PET scanners, the scatter problem becomes even more prominent, and also activity located outside the FOV contributes significantly to the deadtime of the scanner. This is due to the lack of adequate shielding in 3D whole-body imaging compared to 2D imaging. Furthermore, the correction of the data is more complicated. Many of the simple 2D correction algorithms like the convolution subtraction algorithm do not work for 3D [1].

In 2D PET, the shielding between rings restricts the solid angle for scattered events and therefore leads to a significant geometrical suppression of scattered events. However, 3D PET is generally septaless with a large axial FOV. The focus of our study is therefore to investigate the benefits of septa and additional patient shields outside the scanner on our current 3D whole-body PET scanner.

A powerful and widely accepted tool for such examinations are Monte-Carlo (MC) simulations that allow the simulation of real experiments on the computer. In contrast to actual experiments, it is possible to distinguish between scattered and unscattered radiation with MC simulations, and therefore between different count rate contributions. Furthermore, MC simulations are more flexible than experiments, and they help to to reduce the number of experiments, which can be restricted to those that are needed to verify the code.

Additional information on PET and scattered radiation in PET can be found in the proceedings of the First International Workshop on EGS4 [2, 3].

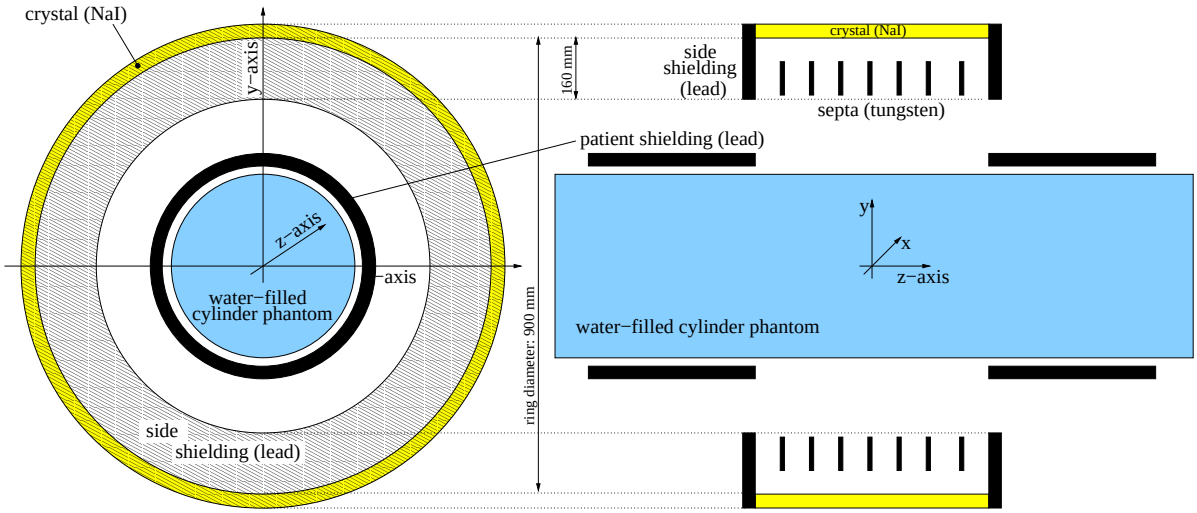

Figure 1: PET scanner geometry. Left) Frontal view, right) axial cross section. The use of the patient shields and the septa are optional.

2 Material and methods

2.1 PET System

The simulated PET scanner was a CPET from ADAC/UGM. It uses 6 curved NaI(Tl) detectors (45×30 cm^2, 2.54 cm thick) with a ring diameter of 90 cm. The axial FOV is 25.6 cm and the transverse FOV is 57.6 cm. The side shielding is 16 cm long and there are no septa. The default energy window for the scanner is currently set at 435 - 665 keV. A detailed description of the scanner can be found in [4, 5].

2.2 Monte-Carlo simulations

Our MC simulations are based on EGS4 [6]. The basic geometric elements which are used to setup the scanner geometry are planes and spheres. These elements are used to model the gantry, NaI detectors and tungsten septa. Figure 1 shows a sketch of the coded geometry.

A complete physical description of the scatter process is very complex and would require too much CPU time to calculate the desired number of histories (typically 10^7 - 10^9). It is therefore necessary to make some simplifying approximations, while still describing the scatter process in a sufficiently accurate way. The approximations give up some accuracy, but reduce the statistical error. The β^+-decay is simulated by two back-to-back photons, each with 511 keV, neglecting the positron range (1-2 mm) and the small non-collinearity of the photon pairs ($\pm0.5^\circ$). Moreover, we restricted the simulations to Rayleigh and Compton scattering, the latter being the predominant interaction the photons undergo at the considered energy. To speed up the simulations we did not simulate the detection process, instead we determined the detection probability of the photon for the undisturbed trajectory in the crystal and counted the photon with this detection probability. We applied several (lower) energy thresholds, from 200 keV to 510 keV in steps of 10 keV. It should be noted that energy smearing of the detected events is available in our code, but was not used for the present study. Events can be rebinned into the sinogram format which is used by our PET scanners. This allows us to process the simulated data like measured data. An event is considered as 'true' or unscattered when neither of the two photons is deflected, and is considered as 'scatter' when one or both photons are scattered.

The cross sections for the different media were generated for an energy range from 50 - 550 keV using PEGS4. Available media are water, lead, tungsten, aluminum, and different scintillator materials, including NaI. Interaction in air was neglected and the vacuum cross section was taken

instead. MC data were obtained by simulating water-filled cylindrical phantoms with diameters up to 50 cm and different lengths. The phantoms contained a point source or a homogeneous activity distribution. The simulations were mainly performed on a SUN Ultra 60 and a SUN ULTRA 10. The simulation of 10^8 histories required approximately 4 hours CPU time, depending on the object and activity distribution.

2.3 Simulated Geometries

2.3.1 Patient Shield: Point source in water-filled cylinders

To investigate the benefits of additional patient shielding, we simulated a point source in a water-filled cylinder (30 cm diameter and 100 cm long) as depicted in Fig. 2. A thickness of 20 mm and a length of 37.2 cm was chosen to achieve the maximum benefits from the shield (the shield completely covers the phantom outside the FOV and 20 mm is thick enough to practically stop all photons in the shield). For each setup, 10^8 histories were simulated.

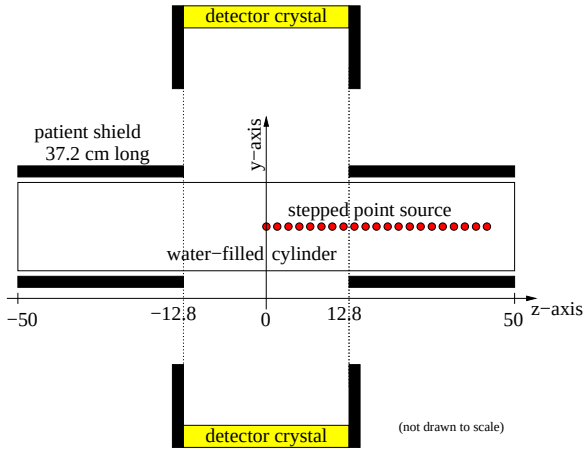

Figure 2: Stepped point source in a water-filled cylinder. The full circles indicate the different axial positions of the point source. The distance between the patient shield and the cylinder was 10 mm, independently of the cylinder diameter. The simulations were performed without and with patient shield (20 mm thick).

2.3.2 Patient Shield: Uniform activity distributions

In a very simple approximation, the activity distribution in a patient can be described as an extended uniform activity distribution. This is justified as long as we consider only global contributions to the scanner countrates. We simulated a uniform activity distribution in 100 cm long water-filled cylinders with diameters ranging from 10 to 50 cm, such that the activity concentration was the same in all phantoms. The length of the patient shield was again 37.2 cm, which completely covers the part of the cylinders that is outside the FOV. In order to compare the simulated patient shield to the best possible shield, we also simulated cylinders with the length of the axial FOV (i.e. where there was no activity outside the FOV).

2.3.3 Length and thickness of the patient shield

In order to determine the minimum length and thickness of the patient shield that are required for an effective shield, we simulated water-filled phantoms ($\varnothing$ = 20 cm) with different lengths (l = 25.6, 51.2, 76.8 cm) and shielding thicknesses (d = 0.32, 0.64, 0.96, 1.32 mm). The 25.6 cm long phantom was centered in FOV, while for the longer phantoms, one end of the phantom was flush with the edge of the FOV, and the other end extended through the scanner and outside the FOV. The length of the patient shield was 25.6 cm which corresponds with the length of the axial FOV. The energy threshold was set to 250 keV.

2.3.4 Septa: Point source in water-filled cylinders

In the current CPET configuration, the rotation mechanism for the ^{137}Cs transmission source uses the 9 cm directly in front of the detector crystal. Therefore, the septa length is limited to 70 mm (see Fig. 1). In the simulations presented below, we used 31 septa, each 60 mm long and 1 mm thick, and they were equally spaced across the axial FOV. The phantom was again the stepped point source in a water-filled cylinder ($\varnothing$ = 30 cm, length = 100 cm, see 2.3.1) and the energy threshold was set to 450 keV.

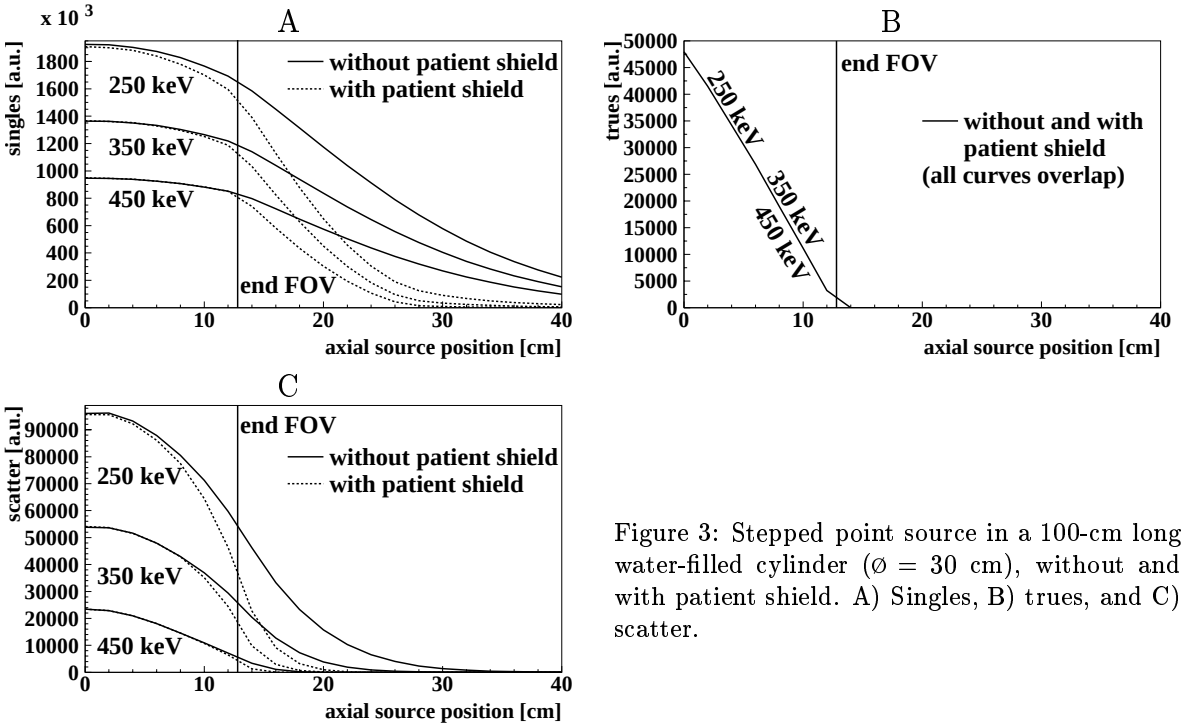

Figure 3: Stepped point source in a 100-cm long water-filled cylinder (ø = 30 cm), without and with patient shield. A) Singles, B) trues, and C) scatter.

2.3.5 Uniform activity distributions

To investigate the impact of septa on a uniform activity distribution, we simulated a water-filled cylinder (length = 76.8 cm) with different diameter d = 20, 30, 40, 50 cm and an energy threshold of 450 keV. The same septa as in 2.3.4 were used. In addition, the simulations were repeated with the patient shields described above.

3 Results and discussion

3.1 Patient Shield

3.1.1 Point source in water-filled cylinders

Independently of the energy threshold, there is a significant singles contribution from activity outside the FOV (see Fig. 3 A). For example, at a distance of 7.2 cm beyond the edge of the FOV (z=20 cm), a point source has a singles countrate of 60.6 % of a point source in the center of the FOV (z=0 cm, LLD=450 keV). At 17.2 cm from the edge of the FOV (z=30 cm), the singles countrate is 28.5 %. If a patient shield is used, the contribution decreases to 32.0 % and 0.8 %, respectively. This leads to the conclusion that patient shields significantly reduce the singles from activity outside the FOV, reducing detector deadtime and randoms. The trues events are not affected by the patient shield and are also independent of the energy threshold, since no energy smearing was applied (see Fig. 3 B). Figure 3 C shows that the effect of the shields on scattered events is nearly negligible for an energy threshold of 450 keV, but increases with decreasing energy threshold. The data for a threshold of 250 keV shows that the patient shield is even effective for source positions inside the FOV, blocking the trajectories for photons reentering the FOV after being scattered outside the FOV.

The results show also that PET scanners like the NaI based CPET with good energy resolution (but limited countrate capability) and a high energy threshold, suffer from outside-the-FOV activity mainly due to single events. PET scanners with poor energy resolution (typically BGO block detector based) and a low energy threshold, but high countrate capability, suffer from outside-the-FOV activity also due to scattered events.

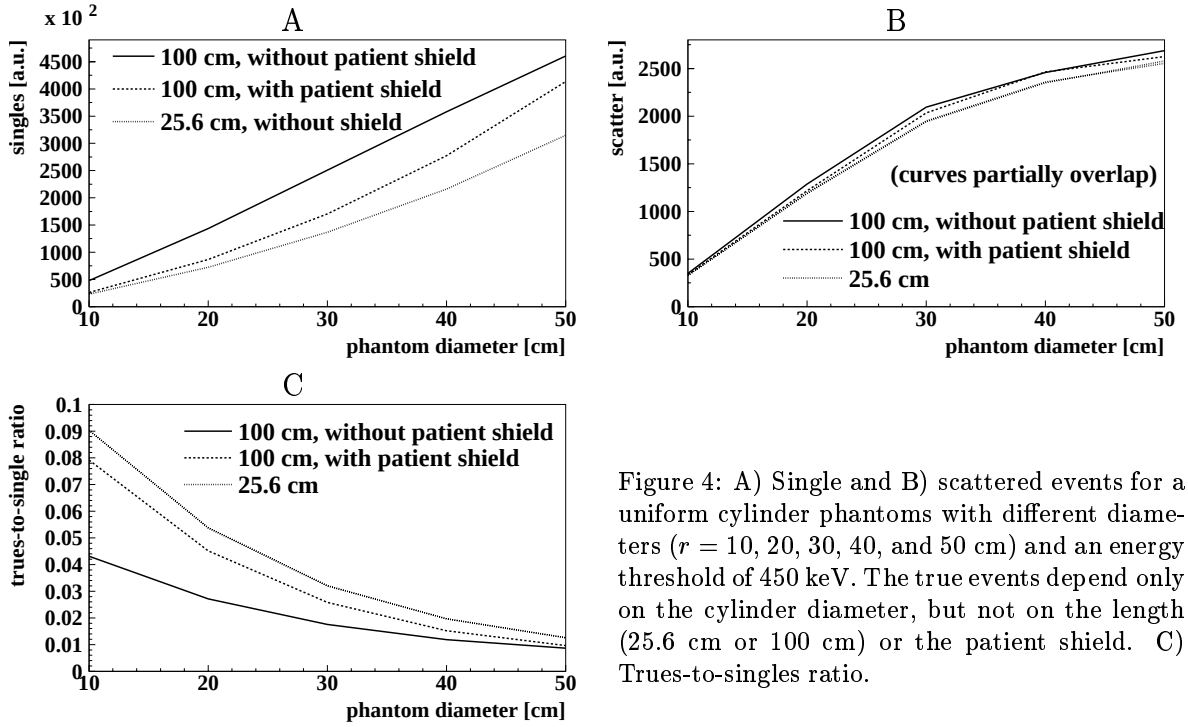

Figure 4: A) Single and B) scattered events for a uniform cylinder phantoms with different diameters (r = 10, 20, 30, 40, and 50 cm) and an energy threshold of 450 keV. The true events depend only on the cylinder diameter, but not on the length (25.6 cm or 100 cm) or the patient shield. C) Trues-to-singles ratio.

3.1.2 Uniform activity distributions

Figure 4 A shows that the patient shield reduces the singles contribution by approximately 45 % for a 10-cm diameter phantom and is nearly as good as the optimum shield (25.6 cm long phantom), which has a singles rate approximately 50 % of that with the 100-cm long phantom. The result is an improvement in the trues-to-singles ratio of more than 80 % due to the patient shield (see Fig. 4 C). The patient shield is most effective for a small phantom diameter and its efficiency decreases with increasing diameter. For a 50 cm diameter phantom, the improvement in the singles rates is only 10 %, while the singles rate for the 25.6 cm long phantom shows a reduction of 30 %. We can also conclude from these data that for the 10-cm diameter phantom (length = 100 cm), 50 % of the singles rate comes from the activity outside the FOV, while for the 50-cm diameter phantom (length = 100 cm) only 30 % of the singles rate comes from outside the FOV. Consequently, the relative contribution from activity outside the FOV becomes less important with increasing object diameter. This is an effect of the change in the scan geometry and the self-attenuation of the object.

As we already learned from the point source simulations above, there is no significant scatter contribution from outside the FOV for an energy threshold of 450 keV. The scatter contributions are very comparable for all three phantom configurations for a given phantom diameter (see Fig. 4 B). Note, this is not true if the threshold is lowered, as it is the case for most BGO based PET scanner.

3.1.3 Length and thickness of the patient shield

Figure 5 shows that the singles contribution and the resulting trues-to-singles ratio are nearly identical for the 51.2-cm and 76.8-cm long phantom, independently of the shielding thickness. From this we conclude that a shielding length of 25.6 cm is sufficient. The number of single events decreases with increasing shielding thickness, and consequently the trues-to-singles improves with increasing shielding thickness, showing an asymptotic behavior. The improvement from a thickness of 0.96 mm to 1.32 mm is only marginal and defines the optimum shielding thickness. As was shown above in the simulations of the point source, increasing the energy threshold only improves the situation and the results can be applied to any higher threshold than 250 keV, in particular 450 keV.

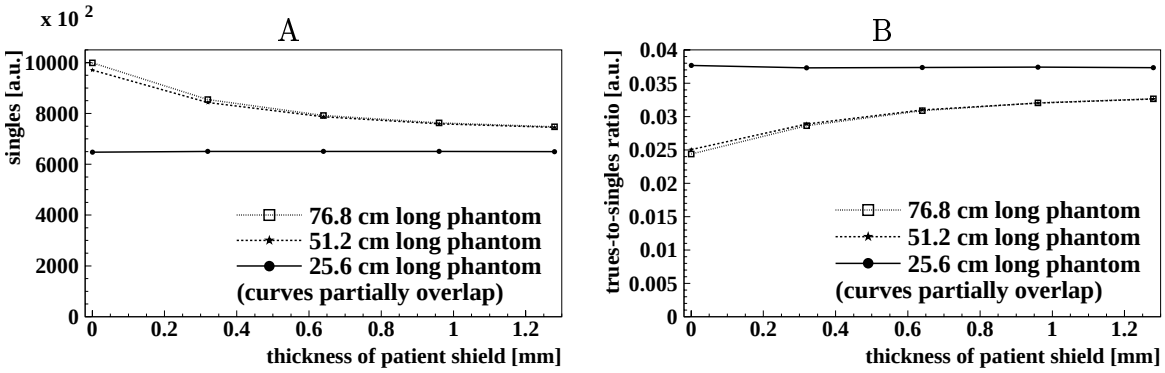

Figure 5: A) Singles contributions and B) trues-to-singles ratio for uniform activity distributions in a water-filled cylinder (ø = 20 cm) as function of the shielding thickness.

3.2 Septa

3.2.1 Point source in water-filled cylinders

Figure 6 shows that septa significantly reduce the singles contribution. For example, the reduction for the center position is 66 %. At the same time, septa also reduce the trues contribution, and the resulting trues-to-singles ratio for septa is lower in the center of the FOV than without septa, but is higher at the edge of the FOV. Overall, septa lead to an axially more uniform trues-to-singles ratio. The biggest impact of the septa is on scattered events; for example, they are reduced by 86 % for the central source position. The scatter fraction (SF), which is defined as

$$SF = \frac{\text{scattered events}}{\text{total events}} \tag{1}$$

is significantly lower with septa than without septa across the FOV. This leads to the conclusion that septa are helpful to reject scattered events, but it is unclear from the point source simulation, if the effect on the trues-to-singles ratio is beneficial, neutral, or negative.

3.2.2 Uniform activity distributions

While it was unclear from the point source simulations if the septa are beneficial for the trues-to-singles ratio or not, Fig. 7 A clearly shows that septa lower the trues-to-singles ratio. This is true for all simulated phantom diameters. The best results for the trues-to-singles ratio can be achieved, if patient shields without septa are used. As expected from the point source simulations, septa help to reduce the scatter fraction and the effect increases with increasing diameter.

4 Conclusions

The use of external patient shields is advantageous, particularly for small objects. Patient shields have no impact on true events and help to reduce scatter contamination from activity inside and outside the FOV. But this only relevant if a low energy threshold is used (e.g. 250 keV). For a high energy threshold (e.g. 450 keV), the simulations showed that the scatter contamination is already suppressed even without the external patient shields. The singles contribution can be reduced up to 25 %, which corresponds to a reduction of random events of 44 % and a reduction of the scanner deadtime by ∼40 % for a typical clinical countrate.

The use of septa can be advantageous for large objects, if the main objective is to reduce scatter and if the loss of true events is compensated for by an increase of the injected activity. The investigated septa reduce the true countrate by ∼ 75 %, but they also reduce the trues-to-singles ratio, particularly for small objects. The reduction of scattered events leads to a decrease of the scatter fraction by 15 % (for small objects) - 30 % (for large objects). It should be noted that septa cause axial inhomogeneities

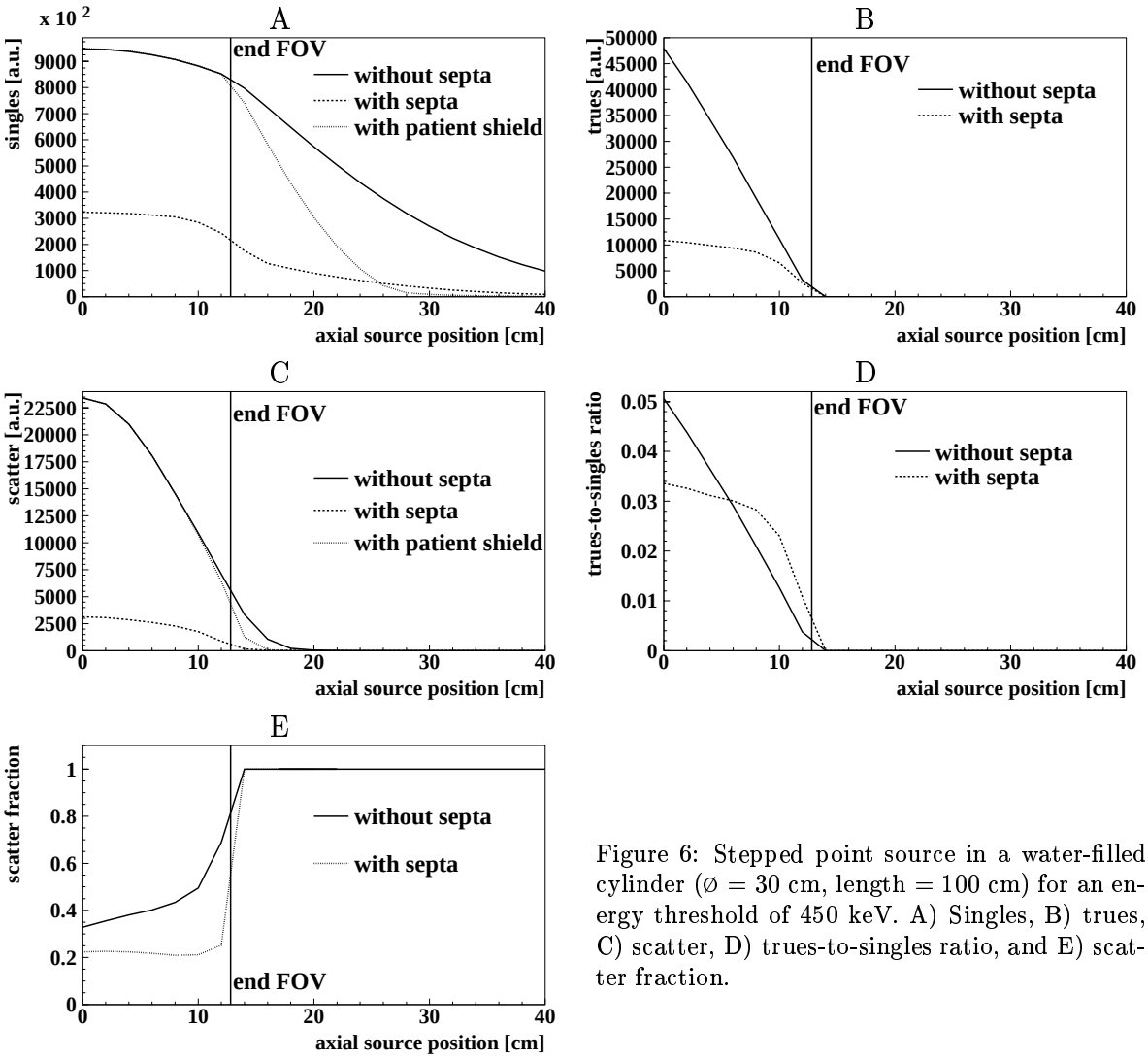

Figure 6: Stepped point source in a water-filled cylinder (ø = 30 cm, length = 100 cm) for an energy threshold of 450 keV. A) Singles, B) trues, C) scatter, D) trues-to-singles ratio, and E) scatter fraction.

in the sensitivity that are a potential problem for data corrections. Further MC simulations are necessary to investigate the effectiveness of septa of varying number, length and thickness.

Acknowledgments

The authors would like to thank Dr. Margaret E. Daube-Witherspoon for her help and suggestions. This work was supported by a grant from the Department of Energy (DE-FG02-88ER60642). Dr. L. E. Adam was supported in part by a Benedict Cassen Postdoctoral Fellowship from the Education and Research Foundation of the Society of Nuclear Medicine.

References

[1] L.-E. Adam, J. S. Karp, and G. Brix, "Investigation of scattered radiation in 3D whole-body positron tmission tomography using Monte Carlo simulations," *Phys. Med. Biol.* **44** (1999)2879–2895.

[2] Y. Narita, M. Shidara, T. Nakumara, T. Fujiwara, and M. Itoh, "Simulation of Compton scatter in 3-dimensional pet," in *Proceedings of the First International Workshop on EGS4*.

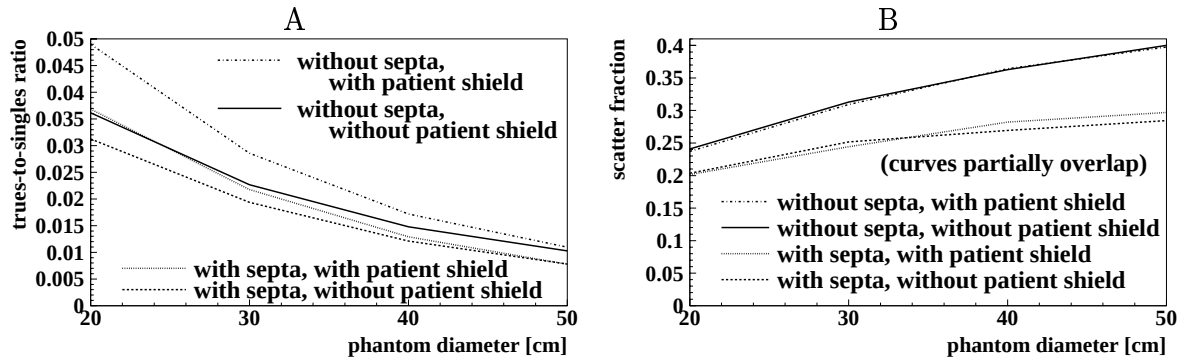

Figure 7: A) Trues-to-singles ratio and B) scatter fraction for uniform, cylindrical phantoms with different diameters (r = 20, 30, 40, and 50 cm) and an energy threshold of 450 keV.

[3] M. Shidara, Y. Narita, T. Nakamura, M. Miyake, T. Fujiwara, and M. Itoh, "A preliminary study of Compton scattering correction in 3D-PET study based on the unfolding method," in *Proceedings of the First International Workshop on EGS4.*

[4] L.-E. Adam, J. S. Karp, and R. J. Smith, "PET camera performance measurements: a comparison between three PET cameras," *J. Nucl. Med.* **40**(1999)76.

[5] L.-E. Adam, J. S. Karp, M. E. Daube-Witherspoon, and R. J. Smith, "Performance of a whole-body PET scanner using curve-plate NaI(Tl) detectors," *(submitted).*

[6] W. R. Nelson, H. Hirayama, and D. W. O. Rogers, *The EGS4 code system. SLAC-Report-265*, Stanford University, Stanford, 1985.